mater.scichina.com link.springer.com

Published online 28 September 2022 | https://doi.org/10.1007/s40843-022-2182-0
Sci China Mater 2023, 66(2): 513–521

Bulk and interface-strengthened $Li_7P_{2.9}Sb_{0.1}S_{10.65}O_{0.15}I_{0.2}$ electrolyte *via* dual-source doping for all-solid-state lithium-sulfur batteries

Bo-Sheng Zhao, Peng Chen* and Xue-Ping Gao*

ABSTRACT **Sulfide solid electrolyte is a promising candidate for the development of high-energy lithium-sulfur (Li-S) batteries. However, the concurrent improvement of ionic conductivity, bulk air stability, and compatibility of the electrolyte/electrode interface of sulfide solid electrolyte remains a huge challenge. Herein, we propose a dual-source doping (Sb_2O_3 and LiI) strategy to prepare a multifunctional sulfide solid electrolyte. Sb_2O_3 can broaden the transmission path of lithium ions and improve the bulk stability, and LiI can inhibit the generation of lithium dendrites and reduce the electrolyte/electrode resistance. Therefore, the sulfide solid electrolyte can be strengthened in terms of its bulk and interface, thus exhibiting a high ionic conductivity of 1.69×10^{-3} S cm^{-1} at 30°C, high air stability, and high electrochemical stability with lithium metal. On this basis, the as-prepared all-solid-state Li-S batteries (ASSLSBs) can exhibit a high specific discharge capacity after being cycled at 0.05 C for 100 cycles at room temperature (833 mA h g^{-1}) or 60°C (949 mA h g^{-1}). This work provides a rational scheme for the preparation of practical sulfide solid electrolytes and high-performance ASSLSBs.**

Keywords: all-solid-state batteries, lithium-sulfur batteries, multifunctional sulfide solid electrolyte, ionic conductivity, air-stability

INTRODUCTION

With the soaring global energy consumption, the development of new energy storage systems with high energy density and high security is urgently needed [1–4]. Lithium-sulfur (Li-S) batteries have become one of the most promising alternatives for next-generation energy storage systems due to their high theoretical energy density (2600 W h kg^{-1}) and high specific capacity (1675 mA h g^{-1}) [5–8]. However, lithium polysulfide can shuttle in the liquid electrolyte during cycling, and the capacity of Li-S batteries decays extremely quickly, which seriously affects their cycle stability [9,10]. Moreover, the lithium metal in the liquid electrolyte will inevitably generate lithium dendrites and cause a short circuit during electrochemical charge-discharge cycles, posing serious safety hazards [11,12]. By contrast, no lithium polysulfide is produced in all-solid-state Li-S batteries (ASSLSBs), which not only eliminates the shuttle effect of lithium polysulfide but also improves the capacity and cycle stability of Li-S batteries [13,14]. Replacing liquid organic electrolytes with non-volatile and non-flammable sulfide solid electrolytes can improve the stability and safety of ASSLSBs fundamentally [15,16]; therefore, the application of sulfide electrolytes has attracted widespread attention.

The properties of solid electrolytes play a decisive role in the performance of ASSLSBs [17,18]. Sulfide solid electrolytes have a high ionic conductivity (>1 mS cm^{-1}), a wide electrochemical stability window (>5 V *vs.* Li/Li$^+$), and good mechanical properties that are highly favorable in ASSLSBs [19–22]. However, some critical issues, such as ionic conductivity, electrolyte stability, and electrolyte/electrode interface compatibility, need to be resolved [23–27]. In ambient air, the sulfide solid electrolyte will be hydrolyzed to release the toxic gas hydrogen sulfide, which destroys the electrolyte structure, leading to decreases in the ion conductivity and degradation of the battery performance [28,29]. Meanwhile, the presence of lithium dendrites at the interface between the solid electrolyte and the anode will cause a rapid short circuit during cycling [30,31]. In general, the bulk and interface of sulfide electrolytes need further optimization for future applications. As previously reported, replacing S^{2-} in the sulfide solid electrolyte with O^{2-} ions can improve the bulk stability of the sulfide solid electrolyte and enhance its inherent air and redox stability [23,32]. In addition, replacing P^{5+} with ions that possess a larger atomic radius or higher polarizability can broaden the lithium-ion transport channel and improve the ionic conductivity of electrolytes [33,34]. In particular, the addition of LiI to sulfide solid electrolytes can not only inhibit the formation of lithium dendrites but also increase the mobility of lithium ions at the interface between the electrolyte and the lithium anode [35,36]. Consequently, the appropriate modification of sulfide electrolyte, especially the implementation of proper doping technologies, may be a practical method for improving battery performance.

In this work, we selected a dual-source doping strategy to optimize the sulfide solid electrolyte. A new type of $Li_7P_{2.9}Sb_{0.1}S_{10.65}O_{0.15}I_{0.2}$ electrolyte was prepared by adding Sb_2O_3 and LiI to the sulfide solid electrolyte through high-energy ball milling and further heat treatment. Compared with the $Li_7P_3S_{11}$ electrolyte, the dual-doped $Li_7P_{2.9}Sb_{0.1}S_{10.65}O_{0.15}I_{0.2}$ electrolyte has higher ionic conductivity, better air stability, and solid-solid interface compatibility and benefits from the strengthened bulk and interface structure. Therefore, the use of $Li_7P_{2.9}Sb_{0.1}S_{10.65}O_{0.15}I_{0.2}$ electrolyte with better chemical and electrochemical properties to assemble ASSLSBs results in higher battery capacity, better rate performance, and cycle stability, showing a promising attempt for the practical use of ASSLSBs.

Institute of New Energy Material Chemistry, School of Materials Science and Engineering, Nankai University, Tianjin 300350, China
* Corresponding authors (emails: chenpengnk@nankai.edu.cn (Chen P); xpgao@nankai.edu.cn (Gao XP))

EXPERIMENTAL SECTION

Preparation of solid-state electrolytes

$Li_7P_{2.9}Sb_{0.1}S_{10.65}O_{0.15}I_{0.2}$ solid-state electrolytes were prepared by a two-step method through high-energy ball milling and roasting. First, the reactants, including Li_2S (99.9%, Alfa Aesar), P_2S_5 (99%, P ≥ 27%, Macklin), Sb_2O_3 (99.99%, Aladdin), and LiI (99.99%, Aladdin), were accurately weighed by stoichiometric ratio. The weighed reactants were poured into a zirconia tank, and high-energy ball milling was performed at a rotation speed of 550 r min^{-1} for 40 h at room temperature. Then, the powders obtained by ball milling were pressed into flakes and calcined at 240°C for 2 h. Finally, $Li_7P_{2.9}Sb_{0.1}S_{10.65}O_{0.15}I_{0.2}$ solid-state electrolytes can be obtained. All the experiments except ball milling were performed in a glove box filled with argon (H_2O <0.1 ppm, O_2 <0.1 ppm). $Li_7P_3S_{11}$ solid-state electrolytes were prepared in accordance with a previously reported article [29].

Preparation of the sulfur-carbon (S-C) composite cathode

Via a simple ball milling method, the active materials of sulfur, carbon (super P) as the electronic conductive additive, and $Li_7P_{2.9}Sb_{0.1}S_{10.65}O_{0.15}I_{0.2}$ solid-state electrolytes as the ionic conductor were weighed and mixed at a ratio of 4:3:3 to prepare the composite cathode (S-C/$Li_7P_{2.9}Sb_{0.1}S_{10.75}O_{0.25}$). First, sulfur active materials and the electronic conductive additive carbon were poured into the zirconia ball at a mass ratio of 4:3 and mechanically ball milled at 350 r min^{-1} for 5 h at room temperature. Then, the S-C composites were mixed with a certain amount of $Li_7P_{2.9}Sb_{0.1}S_{10.65}O_{0.15}I_{0.2}$ solid-state electrolytes in the zirconia ball. The three materials were also mechanically ground at 350 r min^{-1} for 10 h. Finally, the composite cathode was obtained and used in ASSLSBs. The S-C/$Li_7P_3S_{11}$ composite cathode was prepared following the same process as above.

Assembly of ASSLSBs

To assemble the ASSLSBs, we used $Li_7P_{2.9}Sb_{0.1}S_{10.65}O_{0.15}I_{0.2}$ and $Li_7P_3S_{11}$ solid-state electrolytes to separate the active materials of the composite cathode (S-C/$Li_7P_{2.9}Sb_{0.1}S_{10.75}O_{0.25}$ and S-C/$Li_7P_3S_{11}$) and the lithium-indium (Li-In) alloy of the anode. Chiefly, the solid-state electrolytes (130 mg) were placed in a specific mold (diameter of 10 mm) and cold-pressed at a pressure of 380 MPa. Subsequently, the composite cathode (1.5 mg) was evenly dispersed on the upper surface of the electrolyte and pressed together with a pressure of 380 MPa. In addition, the Li-In alloy anode was placed on the other side of the electrolyte. On both sides of the three-layer structure, two stainless steel (SS) sheets were added as current collectors. As a very critical step, the application of 100 MPa pressure to the entire mold at ambient temperature can be used to obtain the ASSLSBs. All the above preparation processes were completed in a glove box with an argon atmosphere (H_2O < 0.1 ppm, O_2 < 0.1 ppm). Fig. 1 shows the schematic structure of an ASSLSB.

Material characterization

Powder X-ray diffraction (XRD) was performed using a Rigaku mini Flex II instrument with Cu Kα radiation at a scanning speed of 10° min^{-1}. The Raman spectra were measured using an SR-500I-A Raman microscope with a 532-nm line. Scanning electron microscopy (SEM, JEOL-JSM7800F) and elemental mapping (energy dispersive spectroscopy (EDS), Bruker Quantax 200) were performed to characterize the morphologies and microstructures of the solid-state electrolytes. A closed container of approximately 5000 mL was equipped with a hydrogen sulfide detector (HJ-BXA-H_2S), solid-state electrolytes, and a small fan. The solid-state electrolytes were exposed to a container with a humidity of 25%–30% at 25°C, and the change in hydrogen sulfide content was detected by the hydrogen sulfide detector. Thermogravimetric analysis (TG, METTLER TOLEDO, TG/differential scanning calorimetry) was used to test the sulfur contents in the composite cathode from 50 to 800°C under an argon atmosphere. X-ray photoelectron spectroscopy measurements were conducted on an Escalab 250Xi (Thermo Fisher Scientific).

Electrochemical measurement

The solid-state electrolyte was cold pressed at 380 MPa in the mold, and two SS plates were used as the symmetrical blocking electrodes. Electrochemical impedance spectroscopy (EIS) of the solid-state electrolyte was performed, and the results were recorded at a frequency range of 1 MHz to 1 Hz with an amplitude of 5 mV using Zahner IM6e at temperatures from 303 to 398 K. The electrochemical window of the solid-state electrolyte was measured by cyclic voltammetry (CV), in which the asymmetric Li/solid electrolyte (SE)/SS battery was tested in the voltage window range of −0.5 to 5 V (Li/Li^+) at a scan rate of 1 mV s^{-1}. The symmetrical batteries (Li/SE/Li or Li-In/SE/Li-In) with solid-state electrolytes were measured at a current density of 0.1/0.2 mA cm^{-2} at room temperature. The LAND battery test system (C2001A, LAND China) can test the performance of a battery through the discharge and charge processes at a current

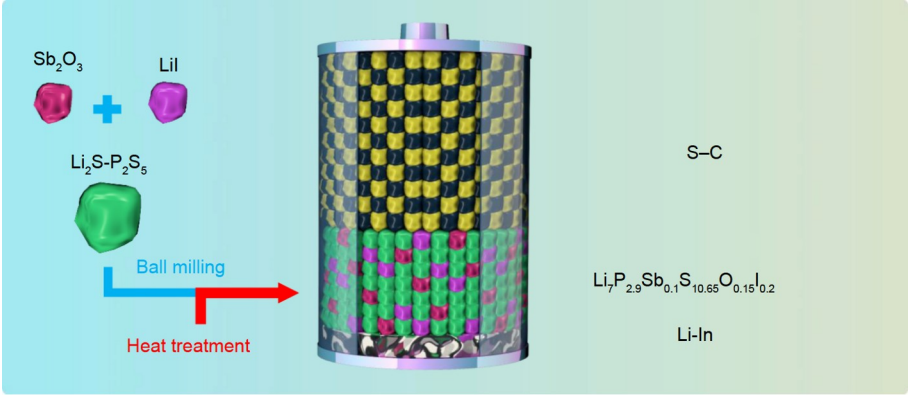

Figure 1 Preparation of solid-state electrolyte and schematic of ASSLSBs.

of 0.05 C with the voltage ranging from 0.8 to 2.4 V (*vs.* Li-In). It can also test the battery at different rates from 0.05 to 1 C at room temperature and 60°C. The specific capacity of ASSLSBs can be obtained by calculating the sulfur active material.

RESULTS AND DISCUSSION

Sb_2O_3 and LiI were doped into the binary electrolyte system of lithium sulfide and phosphorus sulfide by ball milling, and the $Li_7P_{2.9}Sb_{0.1}S_{10.65}O_{0.15}I_{0.2}$ sulfide solid electrolyte with high ionic conductivity was obtained by further heat treatment. The sulfur/carbon composite cathode and lithium indium alloy anode were used to assemble an ASSLSB with the $Li_7P_{2.9}Sb_{0.1}S_{10.65}O_{0.15}I_{0.2}$ sulfide solid electrolyte (Fig. 1).

The powder XRD patterns in Fig. 2a exhibit the crystal structures of Li_2S, P_2S_5, Sb_2O_3, LiI, $Li_7P_3S_{11}$, and $Li_7P_{2.9}Sb_{0.1}S_{10.65}O_{0.15}I_{0.2}$. Comparison of the XRD of the raw materials (Li_2S, P_2S_5, Sb_2O_3, and LiI) and electrolytes ($Li_7P_3S_{11}$ and $Li_7P_{2.9}Sb_{0.1}S_{10.65}O_{0.15}I_{0.2}$) shows that the product electrolytes did not exhibit any of the XRD peaks of the unreacted raw materials, indicating that the crystal structure of the reactants was destroyed, and new crystal-structured electrolytes were formed finally. In addition, the doping elements Sb, O, and I can enter the lattice structure of the $Li_7P_{2.9}Sb_{0.1}S_{10.65}O_{0.15}I_{0.2}$ electrolyte with good crystallinity. Moreover, the diffraction peaks of $Li_4P_2S_6$ can be observed in the $Li_7P_3S_{11}$ electrolyte [37]; however, $Li_4P_2S_6$ was revealed as an impurity with a low conductivity due to the decomposition of $Li_7P_3S_{11}$ during the heat treatment [38,39]. When Sb_2O_3 and LiI were used in doping, the $Li_4P_2S_6$ impurity can hardly be found in the $Li_7P_{2.9}Sb_{0.1}S_{10.65}O_{0.15}I_{0.2}$ electrolyte, indicating that the thermal stability of the $Li_7P_{2.9}Sb_{0.1}S_{10.65}O_{0.15}I_{0.2}$ electrolyte was improved, and the production of the impurity $Li_4P_2S_6$ was suppressed after doping. As a result, the bulk phase purity and stability can be strengthened by dual-source doping.

The Raman spectra in Fig. 2b display the chemical species of $Li_7P_3S_{11}$ and $Li_7P_{2.9}Sb_{0.1}S_{10.65}O_{0.15}I_{0.2}$ electrolytes. Two absorption peaks at 408 and 386 cm^{-1} can be observed in the Raman spectra of $Li_7P_3S_{11}$ electrolytes. Meanwhile, the Raman spectra of $Li_7P_{2.9}Sb_{0.1}S_{10.65}O_{0.15}I_{0.2}$ electrolyte showed three absorption peaks at 416, 406, and 385 cm^{-1}. The absorption peaks at 416 and 408 cm^{-1} were caused by the symmetric stretching vibration of the P–S bond, corresponding to the PS_4^{3-} and $P_2S_7^{4-}$ groups, respectively, indicating that the electrolytes possessed a highly conductive phase [40,41]. The absorption peak of the $P_2S_6^{4-}$ group with a low conductive phase appeared at 386 cm^{-1} [42]. Evidently, the intensity of the absorption peak of the $Li_7P_{2.9}Sb_{0.1}S_{10.65}O_{0.15}I_{0.2}$ electrolyte at 386 cm^{-1} was significantly reduced, indicating that doping with Sb_2O_3 and LiI can effectively reduce the generation of impurity $Li_4P_2S_6$. The Raman analysis results were consistent with the XRD results, which further proved that dual-source doping can improve the ionic conductivity of the electrolyte.

To study the morphology of the electrolytes and the uniformity of doping, we characterized the electrolytes by SEM, element distribution measurements, and linear sweep (Fig. 3). The $Li_7P_3S_{11}$ electrolyte was composed of small pieces, and the distributions of P and S in the electrolyte were very uniform (Fig. 3a). For comparison, most of the $Li_7P_{2.9}Sb_{0.1}S_{10.65}O_{0.15}I_{0.2}$ electrolytes existed as large lumps, which indicated that the agglomeration became more serious during preparation (Fig. 3b). However, the distribution of each element (P, S, O, Sb, and I) in the $Li_7P_{2.9}Sb_{0.1}S_{10.65}O_{0.15}I_{0.2}$ electrolyte was still very uniform, demonstrating that P, S, O, Sb, and I were successfully doped in the $Li_7P_{2.9}Sb_{0.1}S_{10.65}O_{0.15}I_{0.2}$ electrolyte. The result was consistent with that of the XRD analysis.

Ionic conductivity is crucial for solid electrolytes. To measure the ionic conductivity of dual-source-doped sulfide electrolyte, we selected an SS sheet as the ion-blocking electrode to carry out the EIS test of symmetrical SS/SE/SS battery at different temperatures (303, 313, 333, 353, 373, and 393 K). Fig. 4a shows the EIS impedance diagram of the electrolytes ($Li_7P_3S_{11}$ and $Li_7P_{2.9}Sb_{0.1}S_{10.65}O_{0.15}I_{0.2}$) at 30°C. In the comparison of the impedances of the two electrolytes, the impedance of the $Li_7P_{2.9}Sb_{0.1}S_{10.65}O_{0.15}I_{0.2}$ electrolyte was significantly reduced after the doping of Sb_2O_3 and LiI. In addition, the calculated ionic conductivities of the $Li_7P_3S_{11}$ and $Li_7P_{2.9}Sb_{0.1}S_{10.65}O_{0.15}I_{0.2}$ electrolytes were 8.92×10^{-4} and 1.69×10^{-3} S cm^{-1}, respectively. The ionic conductivity was computed using the following formula:

$$\sigma = L/(S \times R), \quad (1)$$

where σ is the ionic conductivity, L is the electrolyte thickness, S the is electrolyte surface area, and R is the electrolyte impedance [43,44]. Notably, the improvement of the ionic conductivity of the $Li_7P_{2.9}Sb_{0.1}S_{10.75}O_{0.25}$ electrolyte was mainly due to the fact that the doping of Sb^{3+} ions with a large ion radius can not only broaden the transmission path of lithium ions but also shield the Coulomb repulsion among S^{2-} ions, thereby easing the transmission of lithium ions [45,46]. Fig. S1 shows the EIS spectra of

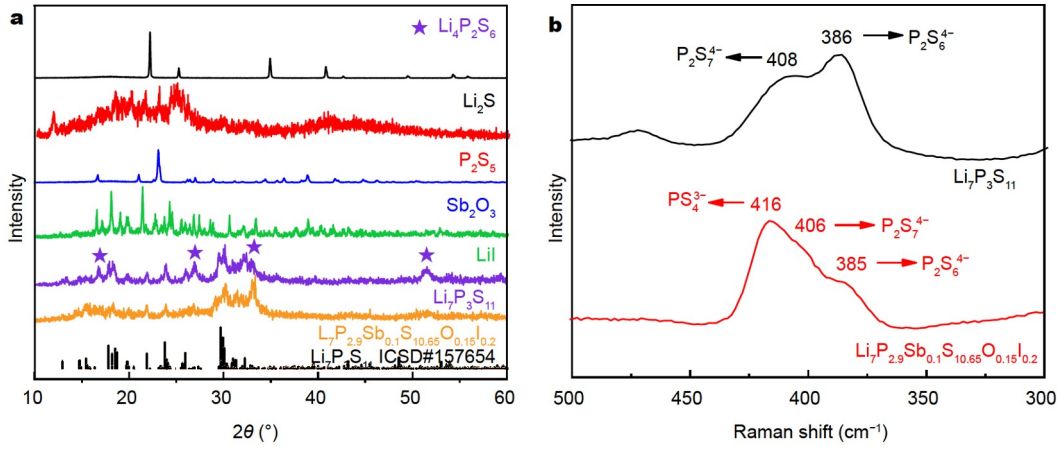

Figure 2 (a) XRD patterns of Li_2S, P_2S_5, Sb_2O_3, LiI, $Li_7P_3S_{11}$, and $Li_7P_{2.9}Sb_{0.1}S_{10.65}O_{0.15}I_{0.2}$. (b) Raman spectra of $Li_7P_3S_{11}$ and $Li_7P_{2.9}Sb_{0.1}S_{10.65}O_{0.15}I_{0.2}$.

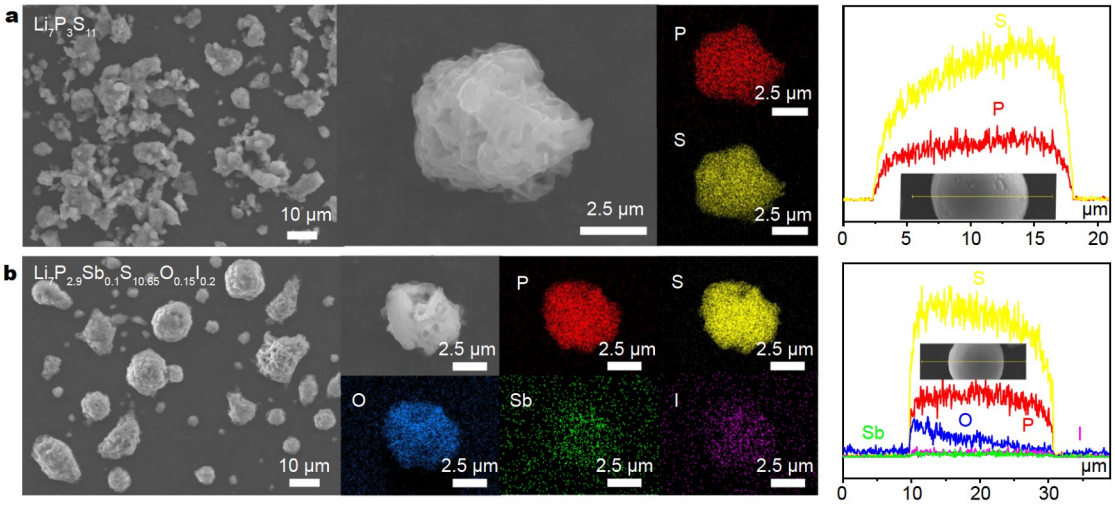

Figure 3 (a) SEM images of $Li_7P_3S_{11}$, EDS mappings of P and S, and linear sweep of $Li_7P_3S_{11}$. (b) SEM images of $Li_7P_{2.9}Sb_{0.1}S_{10.65}O_{0.15}I_{0.2}$, EDS mappings of P, S, O, Sb, and I, and linear sweep of $Li_7P_{2.9}Sb_{0.1}S_{10.65}O_{0.15}I_{0.2}$.

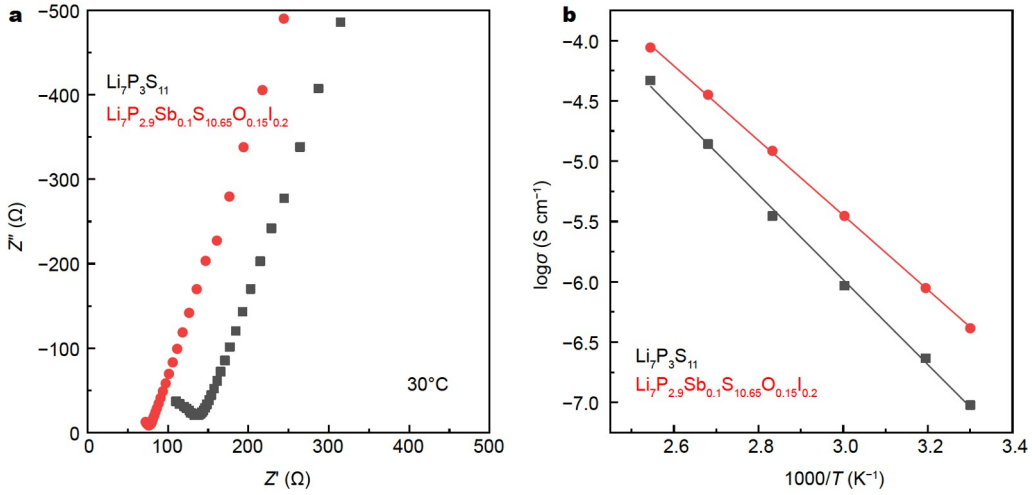

Figure 4 (a) Nyquist plots at 30°C and (b) corresponding Arrhenius plots of the ionic conductivities of $Li_7P_3S_{11}$ and $Li_7P_{2.9}Sb_{0.1}S_{10.65}O_{0.15}I_{0.2}$ electrolytes.

$Li_7P_3S_{11}$ and $Li_7P_{2.9}Sb_{0.1}S_{10.65}O_{0.15}I_{0.2}$ electrolytes at 303, 313, 333, 353, 373, and 393 K, and Fig. 4b presents the results as Arrhenius plots. In addition, the activation energy of the $Li_7P_3S_{11}$ and $Li_7P_{2.9}Sb_{0.1}S_{10.65}O_{0.15}I_{0.2}$ electrolytes can be calculated using the following formula:

$$\sigma = A\exp(-E_a/kT), \quad (2)$$

where σ is the ionic conductivity, T is the absolute temperature, k is the Boltzmann constant, and A is the pre-exponential factor [47,48]. The activation energy of the $Li_7P_{2.9}Sb_{0.1}S_{10.65}O_{0.15}I_{0.2}$ electrolyte is 25.7 kJ mol^{-1}, which is considerably lower than that of the $Li_7P_3S_{11}$ electrolyte (29.3 kJ mol^{-1}). This result indicated the migration of lithium ions in the $Li_7P_{2.9}Sb_{0.1}S_{10.65}O_{0.15}I_{0.2}$ electrolyte and proved that doping with Sb_2O_3 and LiI can improve the lithium-ion conductivity of the electrolyte.

The sulfide solid electrolyte was hydrolyzed to produce the toxic hydrogen sulfide (H_2S) gas in moist air. In bulks, such degradation will damage the structure of the sulfide solid electrolyte and cause a decrease in ion conductivity [49–51]. After dual-source doping, the bulk stability of the sulfide electrolytes can be improved, which was also helpful for air stability. To compare the stabilities of the $Li_7P_3S_{11}$ and $Li_7P_{2.9}Sb_{0.1}S_{10.65}O_{0.15}I_{0.2}$ electrolytes in the air, we exposed the electrolytes in air to monitor the change in H_2S content (Fig. 5a). By comparing the H_2S amount with time, the rate of H_2S production by the $Li_7P_{2.9}Sb_{0.1}S_{10.65}O_{0.15}I_{0.2}$ electrolyte was significantly reduced. Thus, dual-source doping can effectively inhibit the production of H_2S, which is attributed to the tendency of O to form bridging oxygen instead of bridging sulfur [52–54]. Fig. 5b summarizes the total amount of H_2S produced by the electrolytes after 4000 s. The total amount of H_2S produced by the $Li_7P_{2.9}Sb_{0.1}S_{10.65}O_{0.15}I_{0.2}$ electrolyte was 1.13 cm^3 g^{-1}, which accounted for 45% of the total amount of H_2S produced by the $Li_7P_3S_{11}$ electrolyte, showing a significantly improved air stability.

In addition to the bulk stability of the electrolyte itself, the interface of electrolyte/lithium metal is a consistent bottleneck in the use of all-solid-state batteries. Electrochemical stability plays a decisive role in battery performance. Through the CV test at the potential range of −0.5 to 5 V (*vs.* Li/Li$^+$) and the scan rate of 1 mV s^{-1}, the electrochemical window of the $Li_7P_3S_{11}$ and $Li_7P_{2.9}Sb_{0.1}S_{10.65}O_{0.15}I_{0.2}$ electrolytes can be obtained at room temperature. Fig. 6a shows a pair of redox peaks corresponding to the electrochemical deposition ($Li^+ + e^- \rightarrow Li$) and dissolution

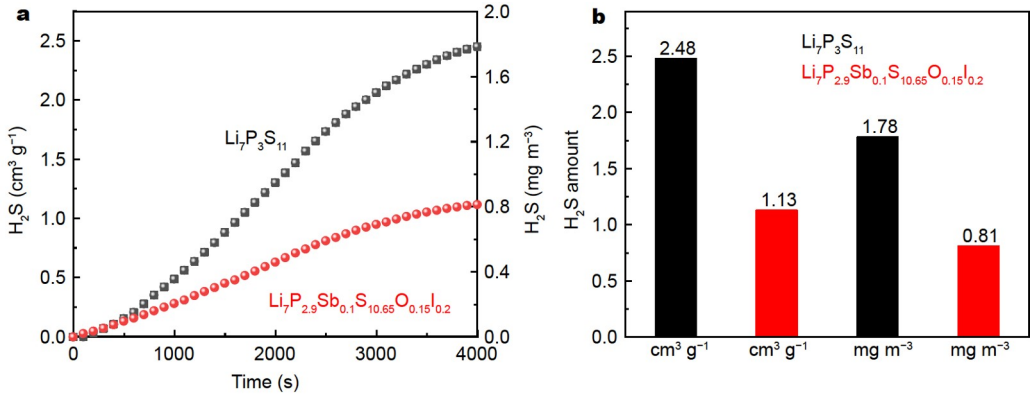

Figure 5 (a) Curve of the amount of H_2S gas produced by $Li_7P_3S_{11}$ and $Li_7P_{2.9}Sb_{0.1}S_{10.65}O_{0.15}I_{0.2}$ electrolytes over time. (b) Total H_2S amount in the $Li_7P_3S_{11}$ and $Li_7P_{2.9}Sb_{0.1}S_{10.65}O_{0.15}I_{0.2}$ electrolytes exposed to the air for 4000 s.

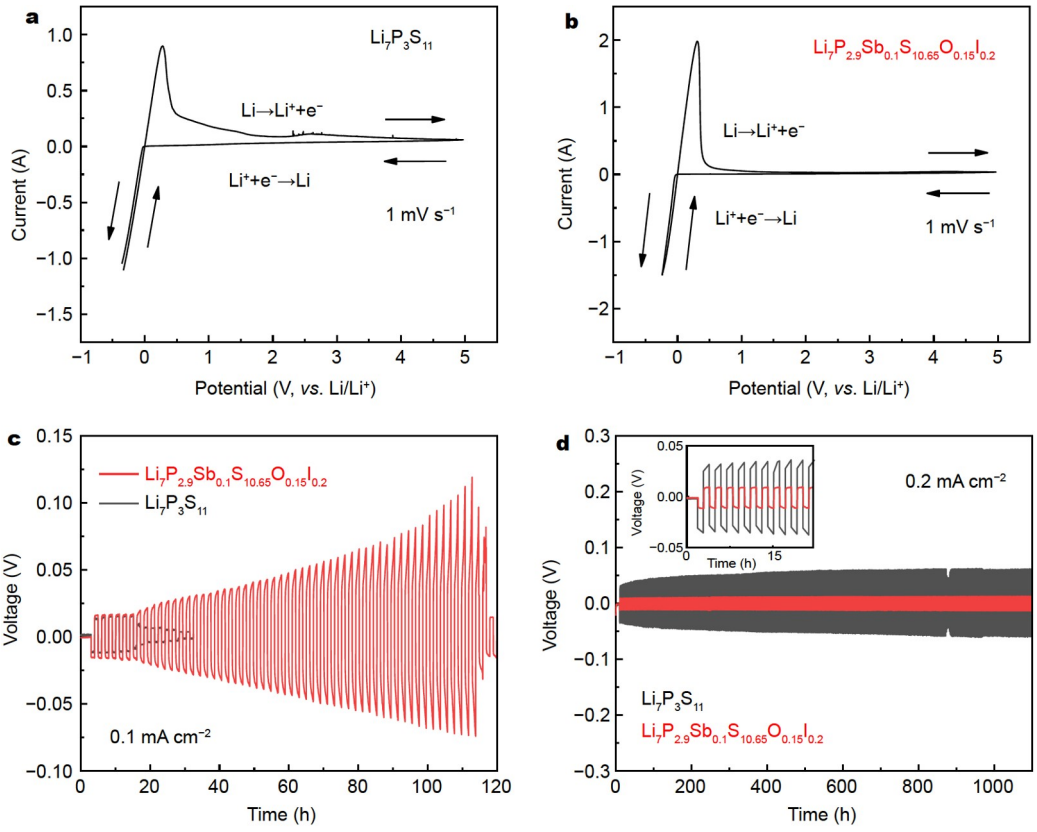

Figure 6 (a and b) CV curves of $Li_7P_3S_{11}$ and $Li_7P_{2.9}Sb_{0.1}S_{10.65}O_{0.15}I_{0.2}$ in the potential range of −0.5 to 5 V (*vs.* Li/Li^+) with a scan rate of 1 mV s^{-1} at room temperature. (c) Galvanostatic charge/discharge curves of the $Li/Li_7P_3S_{11}/Li$ and $Li/Li_7P_{2.9}Sb_{0.1}S_{10.65}O_{0.15}I_{0.2}/Li$ symmetric cells under 0.1 mA cm^{-2}. (d) Galvanostatic charge/discharge curves of Li-In/$Li_7P_3S_{11}$/Li-In and Li-In/$Li_7P_{2.9}Sb_{0.1}S_{10.65}O_{0.15}I_{0.2}$/Li-In symmetric cells under 0.2 mA cm^{-2} at room temperature.

(Li → Li^+ + e^-) of lithium [55]. Given the instability of the $Li_7P_3S_{11}$ electrolyte, a small oxidation peak appeared at 3.8 V (*vs.* Li/Li^+) [56,57]. However, the $Li_7P_{2.9}Sb_{0.1}S_{10.65}O_{0.15}I_{0.2}$ electrolyte only exhibited the electrochemical deposition and dissolution peaks of lithium at the potential range of −0.5 to 5 V (*vs.* Li/Li^+) (Fig. 6b), indicating that the $Li_7P_{2.9}Sb_{0.1}S_{10.65}O_{0.15}I_{0.2}$ electrolyte had better stability, and its electrochemical window reached 5.0 V *vs.* Li/Li^+. Fig. 6c shows the galvanostatic charge and discharge test curve of $Li/Li_7P_3S_{11}/Li$ and $Li/Li_7P_{2.9}Sb_{0.1}S_{10.65}O_{0.15}I_{0.2}/Li$ symmetrical batteries at 0.1 mA cm^{-2} at room temperature. In the beginning, the $Li/Li_7P_3S_{11}/Li$ and $Li/Li_7P_{2.9}Sb_{0.1}S_{10.65}O_{0.15}I_{0.2}/Li$ batteries were stable, and their overpotentials were similar. After 16 h of cycling, the voltage curve of the $Li/Li_7P_3S_{11}/Li$ battery suddenly dropped due to the generation of lithium dendrites, which caused the battery to short circuit [58]. By contrast, although the overpotential of the $Li/Li_7P_{2.9}Sb_{0.1}S_{10.65}O_{0.15}I_{0.2}/Li$ battery gradually increased, the battery can be tested stably for 112 h before the short circuit phenomenon occurred. The assembled Li-In/$Li_7P_3S_{11}$/Li-In and Li-In/$Li_7P_{2.9}Sb_{0.1}S_{10.65}O_{0.15}I_{0.2}$Li-In symmetric batteries were subjected to galvanostatic charge/discharge tests at room temperature and 0.2 mA cm^{-2} to study the stability of the interface between the electrolyte and the

Li-In alloy anode. Fig. 6d shows that the overpotential of the Li-In/$Li_7P_{2.9}Sb_{0.1}S_{10.65}O_{0.15}I_{0.2}$/Li-In battery (+0.011 and −0.010 V) was substantially lower than that of the Li-In/$Li_7P_3S_{11}$/Li-In battery (+0.055 and −0.053 V), and it was very stable in the 1100-h test. This result proved the small interface resistance between the $Li_7P_{2.9}Sb_{0.1}S_{10.65}O_{0.15}I_{0.2}$ electrolyte and the Li-In alloy. Consequently, by dual-source doping, the bulk and interface stability of the $Li_7P_{2.9}Sb_{0.1}S_{10.65}O_{0.15}I_{0.2}$ electrolyte can be improved.

The S-C composite cathode, all-solid-state electrolyte ($Li_7P_3S_{11}$ or $Li_7P_{2.9}Sb_{0.1}S_{10.65}O_{0.15}I_{0.2}$), and Li-In anode were used to assemble ASSLSBs to characterize the electrochemical performance of the electrolyte. The sulfur contents in the cathode were 41.7% and 41.4%, as calculated by TG analysis (Fig. S2a–d). Fig. 7a shows the first-cycle charge/discharge voltage profiles of Li-In/$Li_7P_3S_{11}$/S-C and Li-In/$Li_7P_{2.9}Sb_{0.1}S_{10.65}O_{0.15}I_{0.2}$/S-C batteries in the range of 0.8–2.4 V at room temperature (*vs.* Li-In) and 0.05 C. As the charging and discharging processes of ASSLSBs only involve the conversion between S and Li_2S, only one voltage plateau appeared [59,60]. The polarization of the Li-In/$Li_7P_{2.9}Sb_{0.1}S_{10.65}O_{0.15}I_{0.2}$/S-C battery decreased due to the reduced interface resistance and improved ion conductivity. Therefore, the discharge capacity of the Li-In/$Li_7P_{2.9}Sb_{0.1}S_{10.65}O_{0.15}I_{0.2}$/S-C battery reached 958 mA h g^{-1}, which was considerably higher than that of the Li-In/$Li_7P_3S_{11}$/S-C battery (529 mA h g^{-1}). Fig. 7b displays the rate performances of the Li-In/$Li_7P_{2.9}Sb_{0.1}S_{10.65}O_{0.15}I_{0.2}$/S-C and Li-In/$Li_7P_3S_{11}$/S-C batteries. By comparison, the Li-In/$Li_7P_{2.9}Sb_{0.1}S_{10.65}O_{0.15}I_{0.2}$/S-C battery exhibited a better rate performance than the Li-In/$Li_7P_3S_{11}$/S-C battery. The discharge capacities of the Li-In/$Li_7P_{2.9}Sb_{0.1}S_{10.65}O_{0.15}I_{0.2}$/S-C battery were 970, 889, 740, 541, and 326 mA h g^{-1} at discharge rates of 0.05, 0.1, 0.2, 0.5, and 1 C, respectively. When the rate was reset to 0.05 C, the discharge capacity of the Li-In/$Li_7P_{2.9}Sb_{0.1}S_{10.65}O_{0.15}I_{0.2}$/S-C battery can be restored to 968 mA h g^{-1}, indicating its good reversibility. Fig. 7c presents the cycle performance of the Li-In/$Li_7P_3S_{11}$/S-C and Li-In/$Li_7P_{2.9}Sb_{0.1}S_{10.65}O_{0.15}I_{0.2}$/S-C batteries at a rate of 0.05 C at room temperature. Owing to the unstable solid-solid interface between the electrolyte and cathode/anode, the charging capacity and coulombic efficiency of ASSLSBs in the first cycle were relatively low. However, after the activation process, the battery can work normally and maintain a high coulombic efficiency. The capacity of the Li-In/$Li_7P_3S_{11}$/S-C battery decayed very fast, and the capacity was 85 mA h g^{-1} after 50 cycles of charge and discharge. Notably, the Li-In/$Li_7P_{2.9}Sb_{0.1}S_{10.65}O_{0.15}I_{0.2}$/S-C battery exhibited not only a high specific discharge capacity but also good cycle stability. After 100 cycles of charging and discharging, the specific discharge capacity of the Li-In/$Li_7P_{2.9}Sb_{0.1}S_{10.65}O_{0.15}I_{0.2}$/S-C battery reached 833 mA h g^{-1}, and its coulombic efficiency was 99.94%. Table S1 compares the electrochemical performance

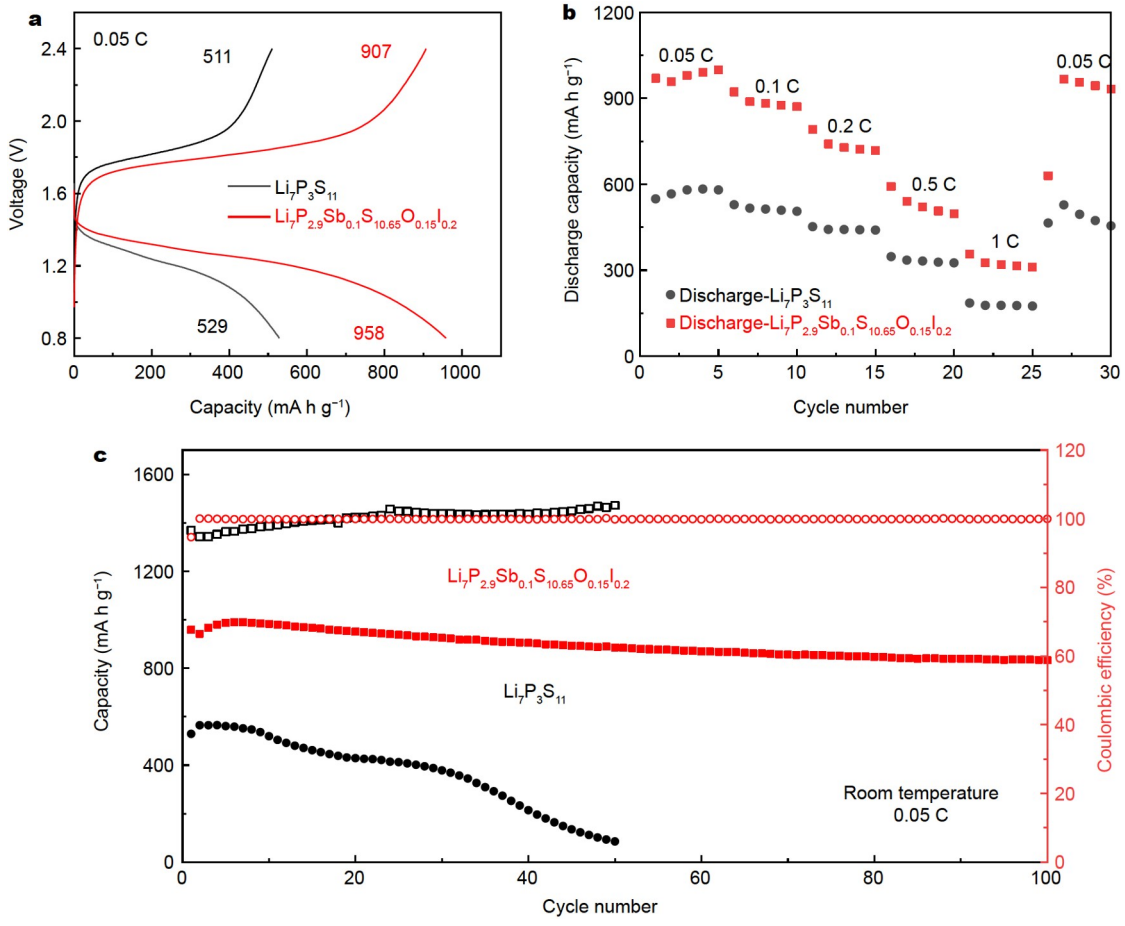

Figure 7 (a) First-cycle charge/discharge voltage profiles of Li-In/$Li_7P_3S_{11}$/S-C and Li-In/$Li_7P_{2.9}Sb_{0.1}S_{10.65}O_{0.15}I_{0.2}$/S-C batteries at 0.05-C discharge rate. (b) Rate performance of Li-In/$Li_7P_3S_{11}$/S-C and Li-In/$Li_7P_{2.9}Sb_{0.1}S_{10.65}O_{0.15}I_{0.2}$/S-C batteries at 0.05, 0.1, 0.2, 0.5, and 1 C. (c) Cycling performance and coulombic efficiency of Li-In/$Li_7P_3S_{11}$/S-C and Li-In/$Li_7P_{2.9}Sb_{0.1}S_{10.65}O_{0.15}I_{0.2}$/S-C batteries at 0.05-C discharge rate.

obtained in this work with that of other previously reported ASSLSBs. Fig. S3 shows the EIS spectra of the Li-In/$Li_7P_3S_{11}$/S-C and Li-In/$Li_7P_{2.9}Sb_{0.1}S_{10.65}O_{0.15}I_{0.2}$/S-C batteries after different cycles. As the number of cycles increased, the impedance of the Li-In/$Li_7P_3S_{11}$/S-C battery increased significantly faster than that of the Li-In/$Li_7P_{2.9}Sb_{0.1}S_{10.65}O_{0.15}I_{0.2}$/S-C battery, indicating that the interface of the Li-In/$Li_7P_{2.9}Sb_{0.1}S_{10.65}O_{0.15}I_{0.2}$/S-C battery had been strengthened. Dual doping can improve the ionic conductivity of sulfide solid electrolytes and ease the transmission of lithium ions. Lithium iodide doping can reduce the interface resistance and inhibit the generation of lithium dendrites. When the sulfide solid electrolyte prepared by dual doping was used to assemble ASSLSBs, the overall impedance of the battery can be reduced, the interface can be stabilized, and the performance of the ASSLSBs can be improved.

The performance of the ASSLSBs at high temperatures is very important. Thus, we opted to charge and discharge the batteries at 60°C. At the high temperature of 60°C, the polarization of the batteries decreased, and only one charging and discharging platform was observed in the first lap (Fig. 8a). The initial discharge capacity of the Li-In/$Li_7P_{2.9}Sb_{0.1}S_{10.65}O_{0.15}I_{0.2}$/S-C battery was 1125 mA h g^{-1}, and that of the Li-In/$Li_7P_3S_{11}$/S-C battery was 803 mA h g^{-1} at 0.05 C. Therefore, the Li-In/$Li_7P_{2.9}Sb_{0.1}S_{10.65}O_{0.15}I_{0.2}$/S-C battery showed a better rate performance (Fig. 8b), and its discharge specific capacity reached 1119, 1037, 953, 842, and 756 mA h g^{-1} at 0.05, 0.1, 0.2, 0.5, and 1 C rates, respectively. Notably, after the rate was adjusted back to 0.05 C, the capacity of the Li-In/$Li_7P_{2.9}Sb_{0.1}S_{10.65}O_{0.15}I_{0.2}$/S-C battery can be restored to 1094 mA h g^{-1}, indicating that the battery had good cycle reversibility. After 100 cycles, the discharge capacity of the Li-In/$Li_7P_3S_{11}$/S-C battery was 74 mA h g^{-1} (Fig. 8c), which was attributed to the partial oxidation and degradation of the electrolyte at 60°C [61–63]. By contrast, the Li-In/$Li_7P_{2.9}Sb_{0.1}S_{10.65}O_{0.15}I_{0.2}$/S-C battery showed excellent performance, and its capacity remained at 949 mA h g^{-1} after 100 cycles. Based on the comparison of the above electrochemical performance, the capacity and stability of the battery assembled with the $Li_7P_{2.9}Sb_{0.1}S_{10.65}O_{0.15}I_{0.2}$ electrolyte have been greatly improved. Thus, the dual-source doping method has good prospects for the development of high-performance solid electrolytes.

CONCLUSIONS

In this work, we mainly prepared high-performance $Li_7P_{2.9}Sb_{0.1}S_{10.65}O_{0.15}I_{0.2}$ electrolytes through dual-source doping strategies and applied them in ASSLSBs. Through the dual-source doping with Sb_2O_3 and LiI, the low conductivity phase inside the $Li_7P_{2.9}Sb_{0.1}S_{10.65}O_{0.15}I_{0.2}$ electrolyte disappeared. Consequently, the ionic conductivity of the $Li_7P_{2.9}Sb_{0.1}S_{10.65}O_{0.15}I_{0.2}$ electrolyte increased to 1.69×10^{-3} S cm^{-1} at 30°C, and the activation energy was reduced to 25.7 kJ mol^{-1}. Moreover, the amount of hydrogen sulfide produced by the $Li_7P_{2.9}Sb_{0.1}S_{10.65}O_{0.15}I_{0.2}$ electrolyte in the air was significantly reduced, and only 1.13 cm^3 g^{-1} was produced after 4000 s. Importantly, the $Li_7P_{2.9}Sb_{0.1}S_{10.65}O_{0.15}I_{0.2}$ electrolyte not only reduced the interface resistance but also greatly improved its stability to Li and Li-In alloy anodes, indicating the strengthened bulk and interface structure. When

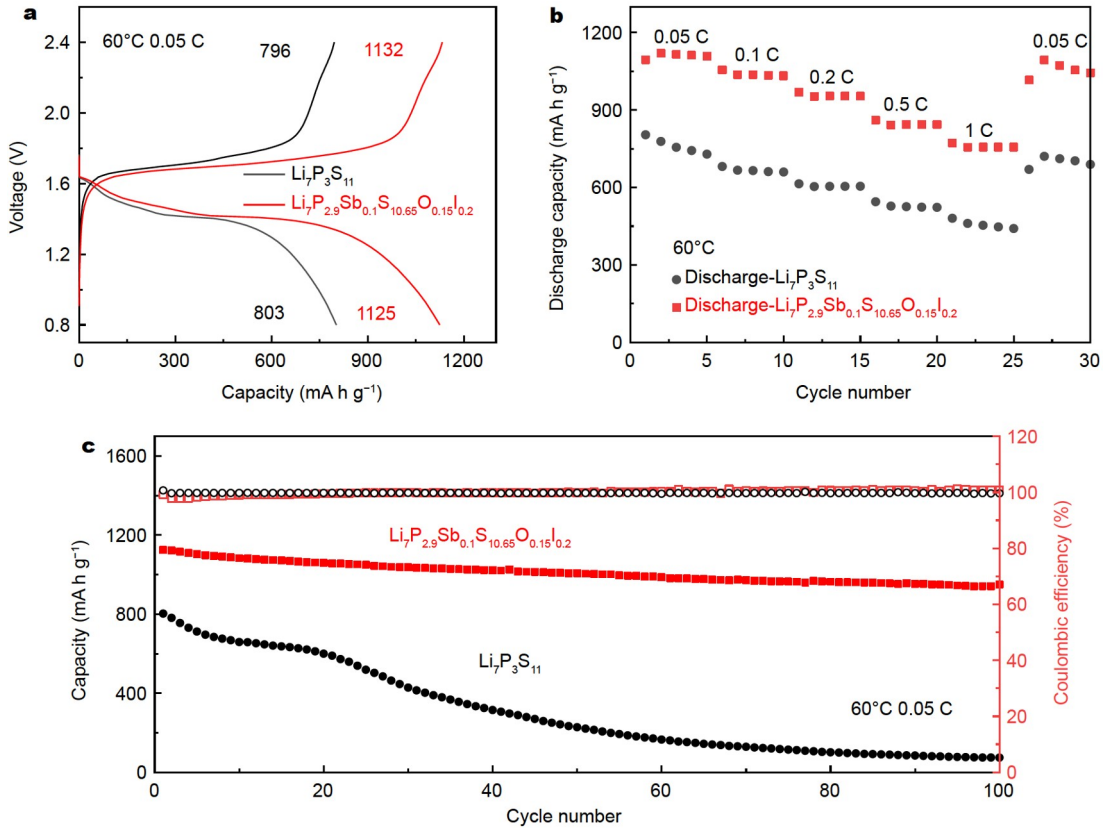

Figure 8 (a) First-cycle charge/discharge voltage profiles of Li-In/$Li_7P_3S_{11}$/S-C and Li-In/$Li_7P_{2.9}Sb_{0.1}S_{10.65}O_{0.15}I_{0.2}$/S-C batteries at 0.05-C rate and 60°C. (b) Rate performance of Li-In/$Li_7P_3S_{11}$/S-C and Li-In/$Li_7P_{2.9}Sb_{0.1}S_{10.65}O_{0.15}I_{0.2}$/S-C batteries at 0.05, 0.1, 0.2, 0.5, and 1 C rates and 60°C. (c) Cycling performance and coulombic efficiency of Li-In/$Li_7P_3S_{11}$/S-C and Li-In/$Li_7P_{2.9}Sb_{0.1}S_{10.65}O_{0.15}I_{0.2}$/S-C batteries (0.05-C rate) at 60°C.

applying the $Li_7P_{2.9}Sb_{0.1}S_{10.65}O_{0.15}I_{0.2}$ electrolyte in ASSLSBs, the discharge capacity remained at 833 mA h g^{-1} after 100 cycles, and the coulombic efficiency was as high as 99.94%. At a high temperature of 60°C, the ASSLSBs also revealed a good discharge-specific capacity and a capacity of 949 mA h g^{-1} after 100 cycles of charge and discharge. In this paper, the dual-source doping strategy strengthened the bulk and interface structure of solid electrolytes, thus improving the electrochemical performance and cycle stability of ASSLSBs and providing a valuable solution for the commercialization of ASSLSBs.

Received 18 April 2022; accepted 6 July 2022; published online 28 September 2022

1 Ji X, Lee KT, Nazar LF. A highly ordered nanostructured carbon-sulphur cathode for lithium-sulphur batteries. Nat Mater, 2009, 8: 500–506
2 Yin YX, Xin S, Guo YG, *et al.* Lithium-sulfur batteries: Electrochemistry, materials, and prospects. Angew Chem Int Ed, 2013, 52: 13186–13200
3 Zhou W, Guo B, Gao H, *et al.* Low-cost higher loading of a sulfur cathode. Adv Energy Mater, 2016, 6: 1502059
4 Fan L, Chen S, Ma R, *et al.* Ultrastable potassium storage performance realized by highly effective solid electrolyte interphase layer. Small, 2018, 14: 1801806
5 Park SW, Oh G, Park JW, *et al.* Graphitic hollow nanocarbon as a promising conducting agent for solid-state lithium batteries. Small, 2019, 15: 1900235
6 Fitzhugh W, Wu F, Ye L, *et al.* Strain-stabilized ceramic-sulfide electrolytes. Small, 2019, 15: 1901470
7 Shen Z, Zhang W, Zhu G, *et al.* Design principles of the anode-electrolyte interface for all solid-state lithium metal batteries. Small Methods, 2019, 4: 1900592
8 Han F, Yue J, Fan X, *et al.* High-performance all-solid-state lithium-sulfur battery enabled by a mixed-conductive Li_2S nanocomposite. Nano Lett, 2016, 16: 4521–4527
9 Yan H, Wang H, Wang D, *et al. In situ* generated Li_2S-C nanocomposite for high-capacity and long-life all-solid-state lithium sulfur batteries with ultrahigh areal mass loading. Nano Lett, 2019, 19: 3280–3287
10 Xu R, Yue J, Liu S, *et al.* Cathode-supported all-solid-state lithium-sulfur batteries with high cell-level energy density. ACS Energy Lett, 2019, 4: 1073–1079
11 Albertus P, Babinec S, Litzelman S, *et al.* Status and challenges in enabling the lithium metal electrode for high-energy and low-cost rechargeable batteries. Nat Energy, 2018, 3: 16–21
12 Zhang K, Lee GH, Park M, *et al.* Recent developments of the lithium metal anode for rechargeable non-aqueous batteries. Adv Energy Mater, 2016, 6: 1600811
13 Li S, Zhang W, Wu Q, *et al.* Synergistic dual-additive electrolyte enables practical lithium-metal batteries. Angew Chem Int Ed, 2020, 59: 14935–14941
14 Zhao Q, Liu X, Stalin S, *et al.* Solid-state polymer electrolytes with in-built fast interfacial transport for secondary lithium batteries. Nat Energy, 2019, 4: 365–373
15 Wang S, Bai Q, Nolan AM, *et al.* Lithium chlorides and bromides as promising solid-state chemistries for fast ion conductors with good electrochemical stability. Angew Chem Int Ed, 2019, 58: 8039–8043
16 Zhang Q, Cao D, Ma Y, *et al.* Sulfide-based solid-state electrolytes: Synthesis, stability, and potential for all-solid-state batteries. Adv Mater, 2019, 31: 1901131
17 Wu J, Liu S, Han F, *et al.* Lithium/sulfide all-solid-state batteries using sulfide electrolytes. Adv Mater, 2021, 33: 2000751
18 Wu J, Shen L, Zhang Z, *et al.* All-solid-state lithium batteries with sulfide electrolytes and oxide cathodes. Electrochem Energ Rev, 2021, 4: 101–135
19 Liu G, Shi J, Zhu M, *et al.* Ultra-thin free-standing sulfide solid electrolyte film for cell-level high energy density all-solid-state lithium batteries. Energy Storage Mater, 2021, 38: 249–254
20 Zhang Z, Wu L, Zhou D, *et al.* Flexible sulfide electrolyte thin membrane with ultrahigh ionic conductivity for all-solid-state lithium batteries. Nano Lett, 2021, 21: 5233–5239
21 Mizuno F, Hayashi A, Tadanaga K, *et al.* New, highly ion-conductive crystals precipitated from Li_2S-P_2S_5 glasses. Adv Mater, 2005, 17: 918–921
22 Zhang Z, Chen S, Yang J, *et al.* Interface re-engineering of $Li_{10}GeP_2S_{12}$ electrolyte and lithium anode for all-solid-state lithium batteries with ultralong cycle life. ACS Appl Mater Interfaces, 2018, 10: 2556–2565
23 Liu G, Xie D, Wang X, *et al.* High air-stability and superior lithium ion conduction of $Li_{3+3x}P_{1-x}Zn_xS_{4-x}O_x$ by aliovalent substitution of ZnO for all-solid-state lithium batteries. Energy Storage Mater, 2019, 17: 266–274
24 Liu G, Weng W, Zhang Z, *et al.* Densified Li_6PS_5Cl nanorods with high ionic conductivity and improved critical current density for all-solid-state lithium batteries. Nano Lett, 2020, 20: 6660–6665
25 Chen S, Xie D, Liu G, *et al.* Sulfide solid electrolytes for all-solid-state lithium batteries: Structure, conductivity, stability and application. Energy Storage Mater, 2018, 14: 58–74
26 Seino Y, Ota T, Takada K, *et al.* A sulphide lithium super ion conductor is superior to liquid ion conductors for use in rechargeable batteries. Energy Environ Sci, 2014, 7: 627–631
27 Su D, Zhou D, Wang C, *et al.* Toward high performance lithium-sulfur batteries based on Li_2S cathodes and beyond: Status, challenges, and perspectives. Adv Funct Mater, 2018, 28: 1800154
28 Zhang Z, Zhang L, Yan X, *et al.* All-in-one improvement toward Li_6PS_5Br-based solid electrolytes triggered by compositional tune. J Power Sources, 2019, 410-411: 162–170
29 Zhao BS, Wang L, Chen P, *et al.* Congener substitution reinforced $Li_7P_{2.9}Sb_{0.1}S_{10.75}O_{0.25}$ glass-ceramic electrolytes for all-solid-state lithium-sulfur batteries. ACS Appl Mater Interfaces, 2021, 13: 34477–34485
30 Garcia-Mendez R, Mizuno F, Zhang R, *et al.* Effect of processing conditions of 75Li_2S-25P_2S_5 solid electrolyte on its DC electrochemical behavior. Electrochim Acta, 2017, 237: 144–151
31 Han F, Zhu Y, He X, *et al.* Electrochemical stability of $Li_{10}GeP_2S_{12}$ and $Li_7La_3Zr_2O_{12}$ solid electrolytes. Adv Energy Mater, 2016, 6: 1501590
32 Ohtomo T, Hayashi A, Tatsumisago M, *et al.* Characteristics of the Li_2O-Li_2S-P_2S_5 glasses synthesized by the two-step mechanical milling. J Non-Crystalline Solids, 2013, 364: 57–61
33 Li X, Liang J, Chen N, *et al.* Water-mediated synthesis of a superionic halide solid electrolyte. Angew Chem Int Ed, 2019, 58: 16427–16432
34 Chen T, Zhang L, Zhang Z, *et al.* Argyrodite solid electrolyte with a stable interface and superior dendrite suppression capability realized by ZnO co-doping. ACS Appl Mater Interfaces, 2019, 11: 40808–40816
35 Lu Y, Tu Z, Archer LA. Stable lithium electrodeposition in liquid and nanoporous solid electrolytes. Nat Mater, 2014, 13: 961–969
36 Ma L, Kim MS, Archer LA. Stable artificial solid electrolyte interphases for lithium batteries. Chem Mater, 2017, 29: 4181–4189
37 Choi SJ, Choi SH, Bui AD, *et al.* LiI-doped sulfide solid electrolyte: Enabling a high-capacity slurry-cast electrode by low-temperature post-sintering for practical all-solid-state lithium batteries. ACS Appl Mater Interfaces, 2018, 10: 31404–31412
38 Xu R, Xia X, Li S, *et al.* All-solid-state lithium-sulfur batteries based on a newly designed $Li_7P_{2.9}Mn_{0.1}S_{10.7}I_{0.3}$ superionic conductor. J Mater Chem A, 2017, 5: 6310–6317
39 Dietrich C, Sadowski M, Sicolo S, *et al.* Local structural investigations, defect formation, and ionic conductivity of the lithium ionic conductor $Li_4P_2S_6$. Chem Mater, 2016, 28: 8764–8773
40 Huang B, Yao X, Huang Z, *et al.* Li_3PO_4-doped $Li_7P_3S_{11}$ glass-ceramic electrolytes with enhanced lithium ion conductivities and application in all-solid-state batteries. J Power Sources, 2015, 284: 206–211
41 Xu R, Xia X, Wang X, *et al.* Tailored Li_2S-P_2S_5 glass-ceramic electrolyte by MoS_2 doping, possessing high ionic conductivity for all-solid-state lithium-sulfur batteries. J Mater Chem A, 2017, 5: 2829–2834
42 Dietrich C, Weber DA, Sedlmaier SJ, *et al.* Lithium ion conductivity in Li_2S-P_2S_5 glasses-building units and local structure evolution during the crystallization of superionic conductors Li_3PS_4, $Li_7P_3S_{11}$ and $Li_4P_2S_7$. J

Mater Chem A, 2017, 5: 18111–18119
43 Zhou L, Tufail MK, Ahmad N, *et al.* Strong interfacial adhesion between the Li_2S cathode and a functional $Li_7P_{2.9}Ce_{0.2}S_{10.9}Cl_{0.3}$ solid-state electrolyte endowed long-term cycle stability to all-solid-state lithium-sulfur batteries. ACS Appl Mater Interfaces, 2021, 13: 28270–28280
44 Seino Y, Nakagawa M, Senga M, *et al.* Analysis of the structure and degree of crystallisation of $70Li_2S$-$30P_2S_5$ glass ceramic. J Mater Chem A, 2015, 3: 2756–2761
45 Wang Y, Lu D, Bowden M, *et al.* Mechanism of formation of $Li_7P_3S_{11}$ solid electrolytes through liquid phase synthesis. Chem Mater, 2018, 30: 990–997
46 Liang J, Chen N, Li X, *et al.* $Li_{10}Ge(P_{1-x}Sb_x)_2S_{12}$ lithium-ion conductors with enhanced atmospheric stability. Chem Mater, 2020, 32: 2664–2672
47 Kaup K, Lalère F, Huq A, *et al.* Correlation of structure and fast ion conductivity in the solid solution series $Li_{1+2x}Zn_{1-x}PS_4$. Chem Mater, 2018, 30: 592–596
48 Yi J, Chen L, Liu Y, *et al.* High capacity and superior cyclic performances of all-solid-state lithium-sulfur batteries enabled by a high-conductivity $Li_{10}SnP_2S_{12}$ solid electrolyte. ACS Appl Mater Interfaces, 2019, 11: 36774–36781
49 Zhang Z, Zhang J, Sun Y, *et al.* $Li_{4-x}Sb_xSn_{1-x}S_4$ solid solutions for air-stable solid electrolytes. J Energy Chem, 2020, 41: 171–176
50 Muramatsu H, Hayashi A, Ohtomo T, *et al.* Structural change of Li_2S-P_2S_5 sulfide solid electrolytes in the atmosphere. Solid State Ion, 2011, 182: 116–119
51 Ohtomo T, Hayashi A, Tatsumisago M, *et al.* Suppression of H_2S gas generation from the $75Li_2S$-$25P_2S_5$ glass electrolyte by additives. J Mater Sci, 2013, 48: 4137–4142
52 Sahu G, Rangasamy E, Li J, *et al.* A high-conduction Ge substituted Li_3AsS_4 solid electrolyte with exceptional low activation energy. J Mater Chem A, 2014, 2: 10396–10403
53 Ahmad N, Zhou L, Faheem M, *et al.* Enhanced air stability and high Li-ion conductivity of $Li_{6.988}P_{2.994}Nb_{0.2}S_{10.934}O_{0.6}$ glass-ceramic electrolyte for all-solid-state lithium-sulfur batteries. ACS Appl Mater Interfaces, 2020, 12: 21548–21558
54 Hayashi A, Muramatsu H, Ohtomo T, *et al.* Improvement of chemical stability of Li_3PS_4 glass electrolytes by adding M_xO_y (M = Fe, Zn, and Bi) nanoparticles. J Mater Chem A, 2013, 1: 6320–6326
55 Park M, Jung HG, Jung WD, *et al.* Chemically evolved composite lithium-ion conductors with lithium thiophosphates and nickel sulfides. ACS Energy Lett, 2017, 2: 1740–1745
56 Zhang Y, Chen R, Liu T, *et al.* High capacity, superior cyclic performances in all-solid-state lithium-ion batteries based on $78Li_2S$-$22P_2S_5$ glass-ceramic electrolytes prepared *via* simple heat treatment. ACS Appl Mater Interfaces, 2017, 9: 28542–28548
57 Zhou L, Tufail MK, Yang L, *et al.* Cathode-doped sulfide electrolyte strategy for boosting all-solid-state lithium batteries. Chem Eng J, 2020, 391: 123529
58 Liu H, Cheng XB, Huang JQ, *et al.* Controlling dendrite growth in solid-state electrolytes. ACS Energy Lett, 2020, 5: 833–843
59 Nagao M, Imade Y, Narisawa H, *et al.* All-solid-state Li-sulfur batteries with mesoporous electrode and thio-LISICON solid electrolyte. J Power Sources, 2013, 222: 237–242
60 Ma Q, Qi X, Tong B, *et al.* Novel $Li[(CF_3SO_2)(n\text{-}C_4F_9SO_2)N]$-based polymer electrolytes for solid-state lithium batteries with superior electrochemical performance. ACS Appl Mater Interfaces, 2016, 8: 29705–29712
61 Kim KJ, Balaish M, Wadaguchi M, *et al.* Solid-state Li-metal batteries: Challenges and horizons of oxide and sulfide solid electrolytes and their interfaces. Adv Energy Mater, 2021, 11: 2002689
62 Lau J, DeBlock RH, Butts DM, *et al.* Sulfide solid electrolytes for lithium battery applications. Adv Energy Mater, 2018, 8: 1800933
63 Xu R, Zhang S, Wang X, *et al.* Recent developments of all-solid-state lithium secondary batteries with sulfide inorganic electrolytes. Chem Eur J, 2018, 24: 6007–6018

Acknowledgements This work was supported by the Science and Technology Support Plan of Tianjin (19YFZCGX00220), the National Natural Science Foundation of China (21935006), and the Fundamental Research Funds for the Central Universities, Nankai University (63211043).

Author contributions Zhao BS, Chen P, and Gao XP conceived the idea. Zhao BS carried out the preparation and electrochemical tests of the devices. Zhao BS, Chen P, and Gao XP co-wrote the paper. All the authors contributed to the general discussion.

Conflict of interest The authors declare that they have no conflict of interest.

Supplementary information Supporting data are available in the online version of the paper.

Bo-Sheng Zhao is currently a PhD candidate at the School of Materials Science and Engineering, Nankai University. His general research interests are in the areas of modifying sulfide solid electrolytes and preparing high-performance all-solid-state lithium-sulfur batteries.

Peng Chen is a lecturer at the School of Materials Science and Engineering, Nankai University. He received his BS degree in 2015 from the College of Chemistry and PhD degree in 2020 from the School of Materials Science and Engineering, Nankai University. His general research interests are in the area of novel energy conversion and storage systems, including solar rechargeable batteries, new types of solar cells, and all-solid-state batteries.

Xue-Ping Gao is a professor at the Institute of New Energy Material Chemistry, Nankai University. He received his doctorate degree from the Department of Chemistry at Nankai University in 1995. He worked as a visiting research fellow at Kogakuin University in Japan from 1997 to 1999. Currently, his main research focuses on energy storage materials for power sources, including lithium-ion, lithium-sulfur, and solar rechargeable batteries.

通过双掺杂增强$Li_7P_{2.9}Sb_{0.1}S_{10.65}O_{0.15}I_{0.2}$电解质用于高性能全固态锂硫电池

赵博生, 陈鹏*, 高学平*

摘要 硫化物固体电解质是发展高容量锂硫电池的理想候选者. 然而, 同时提高硫化物固体电解质的离子导电性、空气稳定性和电解质/电极界面的相容性仍然是一个巨大的挑战. 因此, 我们提出了一种双掺杂(Sb_2O_3和LiI)策略来制备多功能硫化物固体电解质. Sb_2O_3可以拓宽锂离子的传输路径和提高空气稳定性, 而LiI可以抑制锂枝晶的生成和降低电解质/电极之间的电阻. 因此, 硫化物固体电解质在空气中和界面上的性能得到了增强, 在30°C下的离子电导率为1.69×10^{-3} S cm^{-1}, 且具有很好的空气稳定性, 对金属锂也很稳定. 在此基础上, 组装的全固态锂硫电池以0.05 C循环100圈后, 表现出较高的放电比容量(室温, 833 mA h g^{-1}; 60°C: 949 mA h g^{-1}). 本文为制备实用的硫化物固体电解质和高性能全固态锂硫电池提供了合理的方案.

